

Artificial Construction of the Layered Ruddlesden–Popper Manganite $\text{La}_2\text{Sr}_2\text{Mn}_3\text{O}_{10}$ by Reflection High Energy Electron Diffraction Monitored Pulsed Laser Deposition

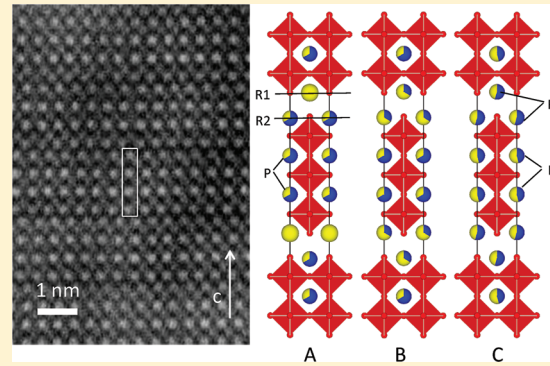
Robert G. Palgrave,[†] Pavel Borisov,[†] Matthew S. Dyer,[†] Sean R. C. McMitchell,[†] George R. Darling,[†] John B. Claridge,[†] Maria Batuk,[‡] Haiyan Tan,[‡] He Tian,[‡] Jo Verbeeck,[‡] Joke Hademann,[‡] and Matthew J. Rosseinsky*,[†]

[†]Department of Chemistry, University of Liverpool, Crown Street, Liverpool L69 7ZD, United Kingdom

[‡]EMAT, University of Antwerp, Groenenborgerlaan 171, B-2020, Antwerp, Belgium

Supporting Information

ABSTRACT: Pulsed laser deposition has been used to artificially construct the $n = 3$ Ruddlesden–Popper structure $\text{La}_2\text{Sr}_2\text{Mn}_3\text{O}_{10}$ in epitaxial thin film form by sequentially layering $\text{La}_{1-x}\text{Sr}_x\text{MnO}_3$ and SrO unit cells aided by in situ reflection high energy electron diffraction monitoring. The interval deposition technique was used to promote two-dimensional SrO growth. X-ray diffraction and cross-sectional transmission electron microscopy indicated that the trilayer structure had been formed. A site ordering was found to differ from that expected thermodynamically, with the smaller Sr^{2+} predominantly on the R site due to kinetic trapping of the deposited cation sequence. A dependence of the out-of-plane lattice parameter on growth pressure was interpreted as changing the oxygen content of the films. Magnetic and transport measurements on fully oxygenated films indicated a frustrated magnetic ground state characterized as a spin glass-like magnetic phase with the glass temperature $T_g \approx 34$ K. The magnetic frustration has a clear in-plane (*ab*) magnetic anisotropy, which is maintained up to temperatures of 150 K. Density functional theory calculations suggest competing antiferromagnetic and ferromagnetic long-range orders, which are proposed as the origin of the low-temperature glassy state.



INTRODUCTION

Vacuum deposition of epitaxial thin films with in situ monitoring by reflection high energy electron diffraction (RHEED) is a technique capable of controlling growth of complex oxides at the unit-cell level.^{1,2} By sequentially depositing an integer number of unit cells of different materials, layered structures can be formed. For example, SrTiO_3 can be constructed by alternately depositing complete monolayers of SrO and TiO_2 .^{3–5} This approach can also be used to deposit films with structures unknown through conventional solid-state synthesis or superlattices, which are wholly unlike materials accessible through normal solid-state synthesis.^{6–10} Such assembly of a desired structure from constituent building blocks under kinetic control can be seen as analogous to organic and inorganic molecular synthesis and represents an opportunity in the field of synthetic solid-state chemistry that has great potential for discovery of new materials and properties.

The $(\text{AO})(\text{ABO}_3)_n$ Ruddlesden–Popper (RP) series of oxides, with their layered structure of $n\text{ABO}_3$ perovskite blocks separated by a single rock salt layer along the (001) direction (Figure 1), are ideal candidates for layer-by-layer assembly. RP structures are of general interest as they permit the introduction

of rock salt layers to control the interactions between electronically or magnetically active perovskite layers. While structures with $n > 2$ are rarely able to be produced through conventional ceramic synthesis, examples with $n \leq 6$ have been grown epitaxially, and in addition the incorporation of different perovskite blocks within the RP structure is possible.^{3,5,11–13} A set of compounds that has attracted great attention is the $(\text{SrO})(\text{La}_{(1-x)}\text{Sr}_x\text{MnO}_3)_n$ series, where the mixed valence manganite perovskites $\text{La}_{(1-x)}\text{Sr}_x\text{MnO}_3$, which are well-studied compounds with a rich magnetic phase diagram, can be further modified by the introduction of nonmagnetic SrO layers. This is of particular interest for $x = 0.33$ $\text{La}_{0.67}\text{Sr}_{0.33}\text{MnO}_3$ (LSMO), which is the archetypal colossal magnetoresistive oxide. The structural, magnetic, and magnetoresistive properties of the $n = 1,2$ RP phases derived from $\text{La}_{(1-x)}\text{Sr}_x\text{MnO}_3$ have been mapped out in detail across the entire composition range $0 \leq x \leq 1$.^{14–21} While the $n = 1$ phase shows no ferromagnetic ordering at any composition, in the region of $x = 0.33$ the $n = 2$ member is a ferromagnetic metal, which displays low field magnetoresistance due to the weak field-tunable coupling between the

Received: November 28, 2011

Published: March 30, 2012

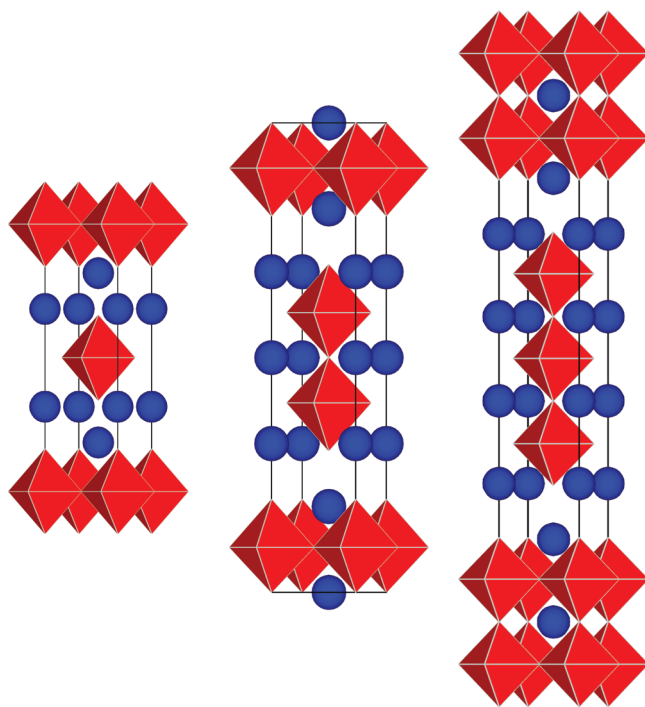


Figure 1. $(\text{SrO})(\text{La}_{(1-x)}\text{Sr}_x\text{MnO}_3)_n$ Ruddlesden–Popper structures with $n = 1$ (left), $n = 2$ (center), and $n = 3$ (right). The La/Sr A cations are represented as blue spheres and the Mn as red oxygen coordination octahedra.

perovskite bilayers.²² The $n = 3$ member of this series appears to be inaccessible at any x value in the $\text{La}_{(1-x)}\text{Sr}_x\text{MnO}_3$ -derived family by conventional ceramic synthesis at high temperature, so its magnetic ground state is of considerable interest.

Despite the high level of interest in layered LSMO-derived manganites generally, there have been only a few reports of attempted artificial construction of such materials, and these have been limited to the $n = 1, 2$ phases, which are already known in the bulk. Tanaka and Kawai deposited $(\text{SrO})\text{(LSMO)}_2$ with $x = 0.4$ using a PLD protocol based on deposition from LSMO and metallic Sr targets.²³ Their films showed the expected ferromagnetic ordering. Recently, MBE has been used to deposit the $n = 1, x = 0.33$ compound by sequentially depositing SrO, LaO, and MnO_2 layers, resulting in high-quality films where the A site ordering was controlled through the deposition process.²⁴ While use of layer-by-layer assembly has been limited, PLD growth of $n = 2$ RP manganite phases from single phase targets has been undertaken by several groups, and generally leads to greater structural quality as assessed by X-ray diffraction (XRD).^{25–27} Typically high substrate temperatures (around 900 °C) are needed to allow formation of the desired large c parameter phase, because considerably more atomic rearrangement is required in the out-of-plane direction as compared to the growth of simple perovskite blocks or rock salt layers. Matvejeff et al. deposited Ru doped and undoped $(\text{SrO})\text{(LSMO)}_2$ using RHEED monitoring to help understand the complex growth mode, caused by large-scale rearrangements of the growing film to form the $n = 2$ material.^{28,29} Other forms of deposition such as sputtering or spray pyrolysis are also able to form $n = 2$ RP films from stoichiometric starting materials.^{30–32}

Here, we report the synthesis of the $n = 3, x = 0.33$ material (this specific composition is referred to throughout as RP3) using RHEED monitored layer-by-layer thin film growth of

three unit cells of LSMO followed by a single atomic layer of SrO. The films were deposited on SrTiO_3 (STO) (001) single crystals. The ab plane of the RP3 structure resembles the perovskite structure, so this plane epitaxially matches the substrate, resulting in RP3 films with the long c axis out of plane. Because the target phase is not known in the bulk, lattice mismatch cannot be calculated exactly, but assuming the RP3 phase inherits the bulk $x = 0.33$ LSMO parameters,¹⁷ then mismatch with STO is +0.77%, that is, slight tensile strain. The stability of the resulting material is understood in terms of the energetics revealed by DFT calculations and found to be due to kinetic trapping of the layered structure rather than epitaxial strain stabilization. At this composition, in the structure accessed through the layer-by-layer growth, the magnetic ground state is not the ferromagnetic one adopted by the $n = 2$ and $n = \infty$ materials, but rather an anisotropic glassy magnetic ordering is observed that is similar to the ground state of the $n = 1, x = 0.33$ phase.

EXPERIMENTAL SECTION

Pulsed laser deposition (PLD) experiments were performed with a Neocera PLD instrument. Growth was monitored with a double-differentially pumped high pressure reflection high energy electron diffraction (RHEED) system supplied by STAIB, Germany. Polycrystalline LSMO and SrO targets were fabricated using standard high temperature ceramic synthesis. To synthesize LSMO, La_2O_3 , MnO_2 , and SrCO_3 were weighed in appropriate amounts, ground, pressed into a pellet, and densified using a cold isostatic press, then fired at 1300 °C in air for 52 h. To form a SrO target, SrO was pressed biaxially in an Ar glovebox, and the resulting pellet was annealed under flowing N₂ at 1150 °C for 12 h. The target was stored in an Ar drybox while not in use. Because of the nature of the PLD apparatus, while loading the SrO target into the chamber, transfer through air was unavoidable. To mitigate the effects of this on the target, laser ablation was used to remove surface SrCO_3 and $\text{Sr}(\text{OH})_2$ contamination after installation of the target and before each deposition. The phase and composition of each target were checked using powder X-ray diffraction (XRD) and energy dispersive X-ray (EDX) analysis, respectively. STO (001) oriented single crystal substrates with miscut <0.2° were supplied by PiKem Ltd. Substrates were cleaned ultrasonically in acetone and ethanol. A TiO₂ terminated surface was produced using the method of Koster et al.,³³ which is as follows. Cleaned substrates were treated ultrasonically in Millipore water for 15 min to form a hydroxylated surface. Substrates were then placed in NH₄F buffered HF solution of pH 5 for 30 s, rinsed in Millipore water, then annealed in air at 950 °C for 1 h. Atomic force microscopy of such treated substrates revealed a step and terrace pattern characteristic of singly terminated surface (see Supporting Information, Figure S1).³³ After introduction to the PLD chamber, substrate surface quality was assessed using RHEED. The RHEED gun was operated at 30 kV, and the incidence angle with the sample surface was <3°. The desired growth atmosphere (0.7–10 mTorr O₂) was set using a mass flow controller and the targets ablated using a 248 nm KrF excimer laser with a pulse repetition rate of 1–20 Hz. RHEED monitoring was carried out by measuring the intensity of the in-phase specular reflection along a [110] azimuth. The number of pulses required for a monolayer of LSMO and SrO was around 120 and 40, respectively, although for each individual deposition the exact pulse number was determined using in situ RHEED, as described in detail below. When using different laser repetition rates, the laser voltage was altered to maintain the same pulse energy, as measured by an in-line energy meter. After the deposition was complete, films were held at the growth temperature, and the oxygen pressure increased to 150 Torr. The films were then cooled at a rate of 20 °C/min under this atmosphere. After cooling, samples were stored in a desiccator. Magnetic properties were measured using a Superconducting Quantum Interference Device (SQUID) magnetometer from

Quantum Design (MPMS-7S). Diamagnetic background signals from the substrates were measured on single SrTiO_3 (001) crystals. To remove possible ferromagnetic contamination, crystals have been annealed in air for 2 h at 650 °C as described by Yee et al.³⁴

Resistivity measurements were performed in a MPMS-7S cryostat using the External Device Control (EDC) option together with Quantum Design Manual Insertion Utility Probe and an attached Keithley model 6430 Sub-Femtoamp Remote SourceMeter. Thin film samples were measured by the four-point probe technique in van der Pauw configuration with the current in-plane. Electric connections were made by silver paint on sputtered gold electrodes.

Samples for transmission electron microscopy (TEM) investigation were made by making cross sections of the film, gluing two cross section together with the films facing each other, and polishing this down to an approximate thickness of 20 μm , after which the sample was further thinned by ion milling (4 kV, +8° and -8°) until transparency for TEM was achieved.

STEM/EELS was carried out on the Qu-Ant-EM system at the University of Antwerp. It consists of a double aberration corrected FEI Titan³ (equipped with GIF quantum) operating at 300 keV. The EELS energy resolution is approximately 1.1 eV. The Mn oxidation state was determined from the exact energy onset of the Mn L_{2,3} edge as well as its energy loss near edge structure (ELNES). The convergence angle was 21 mrad, and the collection angle was approximately 100 mrad. The high angle annular dark field (HAADF) signal was recorded simultaneously.

Further high angle annular dark field scanning transmission electron microscopy (HAADF-STEM) images were acquired using an FEI Tecnai G2 electron microscope operating at 200 kV. All of the experimental images were filtered (background subtraction in Fourier space) using the ImageJ software to increase the signal-to-noise ratio.

■ COMPUTATIONAL DETAILS

To gain further insight into the relative stabilities, structural, electronic, and magnetic properties of LSMO, $(\text{SrO})(\text{LSMO})_2$, and $(\text{SrO})(\text{LSMO})_3$, we carried out periodic density functional theory (DFT) calculations. All calculations were carried out using the VASP code,³⁵ the PBE functional,³⁶ and the projector augmented wave method of treating core electrons.³⁷ The 4s and 4p states of Sr were treated as valence electrons, along with the outer shell electrons of all elements. A planewave energy cutoff of 500 eV and a $3 \times 3 \times 3$ k -point grid were found to give sufficiently converged results and were used throughout. We have used ferromagnetic ordering of the Mn spins, in agreement with the known ground-state ordering of LSMO and $(\text{SrO})(\text{LSMO})_2$ at the $x = 0.33$ doping level.^{22,38}

The La and Sr ions are expected to be disordered over the crystallographic sites of all three oxides. To simulate this disorder using periodic calculations, we follow the work of Zheng and Binggeli on the perovskite LSMO,³⁹ in which La and Sr ions are distributed reasonably homogeneously within a supercell. In our calculations, we use $3 \times 3 \times 3$ supercells for LSMO and $3 \times 3 \times 1$ supercells for $(\text{SrO})(\text{LSMO})_2$ and $(\text{SrO})(\text{LSMO})_3$. For LSMO, La and Sr ions were randomly distributed in the supercell. For the Ruddlesden–Popper materials, the La and Sr ions were randomly distributed within each layer. Five different supercells were used for each composition, each with a different La/Sr ion distribution, and the results averaged to give a mean and standard deviation for all quantities.

Geometry optimization of the ionic positions was performed for every structure until forces on the nuclei were less than 0.01 eV/Å. The cell vectors of the LSMO supercells were also fully optimized. However, the in-plane cell vectors of the Ruddlesden–Popper materials were fixed at the calculated cell parameter of STO (3×3.94 Å) to model the strain imposed by growth on this substrate. The out-of-plane lattice parameter was then varied in intervals of 0.01 Å, with ionic positions optimized each time, until a minimum energy value was obtained.

■ RESULTS

Growth. The overall approach to deposit the target material $\text{La}_2\text{Sr}_2\text{Mn}_3\text{O}_{10}$ (RP3) was to sequentially deposit one atomic layer of SrO followed by three unit cells of LSMO. Artificial construction using RHEED monitored PLD requires layer-by-layer growth of each component as well as low bulk diffusion: fast bulk diffusion perpendicular to the substrate will degrade the deposited layered structure behind the growth front, destroying the desired structure. Layer-by-layer growth occurs within a certain window of adatom surface mobility, which is strongly influenced by substrate temperature.⁴⁰ However, at higher temperatures, bulk diffusion increases, and therefore selection of growth temperature is a compromise between these two factors. We found that RP3 was able to form at a substrate temperature of 700 °C and at pressures from 0.7 to 10 mTorr.

Initially, the growths of LSMO and SrO under these conditions were investigated separately. In the case of LSMO, RHEED oscillations were observed over a wide range of conditions, and stoichiometric cation transfer from target to film was confirmed by growth of 400 nm thick LSMO films followed by EDX analysis. Films grown under these conditions showed the nominal cation stoichiometries within error, and the film grown at 10 mTorr showed an out-of-plane pseudocubic lattice parameter of 3.83 Å, reduced from the bulk pseudocubic parameter due to tensile epitaxial strain, closely corresponding to that reported elsewhere.^{41,42} No significant change in the lattice parameter was found after annealing at 800 °C in air for 10 h, indicating that the film was close to full oxygen stoichiometry.⁴¹ The film showed low temperature resistivity of 5000 $\mu\Omega$ cm and ferromagnetic (FM) ordering with a saturation magnetization of 2.1 μ_B/Mn ion at 5 K and a T_C of 314 K, somewhat lower than reported for optimized LSMO thin film samples, which typically show Curie temperatures close to the bulk value of 370 K.^{43–46} It is important to note that our LSMO films are grown at conditions optimal for artificial construction of RP3, rather than for thick monolayers of LSMO. Nonoptimized deposition conditions, especially the use of lower growth temperatures, are known to produce LSMO films, which, while they are both cation and anion stoichiometric, show ferromagnetic T_C and transport properties that differ significantly from the bulk due to extrinsic factors.^{47–51} In addition, dependence on thin film thickness can also play a significant role.⁵¹ Indeed, after annealing in air at 800 °C, the T_C in our samples increased to 336 K and the resistivity fell to 600 $\mu\Omega$ cm, despite no change in the cation or, as implied by the invariant lattice parameter, anion stoichiometry.

SrO was grown separately onto TiO_2 terminated STO and onto a LSMO buffer layer. In both cases, one complete RHEED oscillation was observed, with preservation of the 2D surface features of the RHEED pattern. Extended growth of SrO far beyond one monolayer led to a spotty RHEED pattern indicative of a 3D surface, as did growth of SrO at significantly higher pressures (>100 mTorr). Our group and others have noted in previous reports of artificial RP growth that “inverted” RHEED oscillations can occur during deposition of rocksalt AO layers onto perovskite surfaces.^{3,11,12} In the present samples, this was only observed when SrO was deliberately grown onto a half-completed layer of LSMO. Comparison of SrO growth onto these different surfaces is shown in the Supporting Information, Figure S2.

STEM EELS was carried out to assess the initial growth of LSMO on nominally TiO_2 terminated STO (001) substrates, as well as subsequent SrO growth atop the LSMO layers. Figure 2

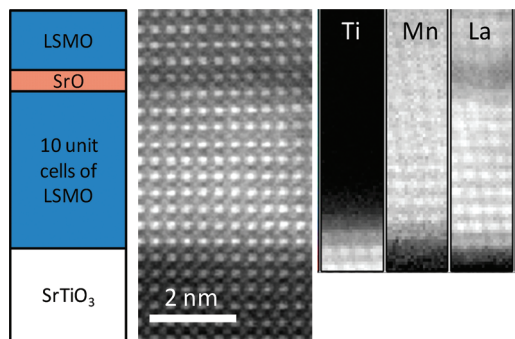


Figure 2. STEM images and EELS maps of an $\text{La}_2\text{Sr}_2\text{Mn}_3\text{O}_{10}$ RP3 film grown at 2 mTorr consisting of a 10 unit cell LSMO buffer layer, followed by a SrO layer, followed by further LSMO deposition (shown schematically on the left). The HAADF STEM image (center) shows the film substrate interface. The EELS maps (right) for Ti, Mn, and La indicate the position of the film substrate interface and show that the film growth begins with a $(\text{La},\text{Sr})\text{O}$ layer. The single deposited SrO layer, which appears as a dark layer on the HAADF image and the La EELS map, can be seen to continue the perovskite structure due to BO_2 termination of the SrTiO_3 substrate and initial LSMO layers. Samples with LSMO buffer layers were not used in magnetic measurements.

shows a cross-sectional HAADF STEM image of the film substrate interface for a film grown consisting of 10 unit cells of LSMO deposited onto TiO_2 terminated STO, followed by a single layer of SrO, then followed by further LSMO deposition. It can be seen that the initial LSMO deposition begins with a $(\text{La},\text{Sr})\text{O}$ layer, indicating that the substrate surface was BO_2 terminated as expected. It can also be seen that the SrO layer, which appears darker in the HAADF image due to its lower atomic mass, continues the perovskite structure, rather than forming a rock salt inclusion to the perovskite layering as found in of RP structures. This is expected if the LSMO is BO_2 terminated, that is, if it preserves the termination of the substrate. It should be noted that samples used for magnetic measurements did not have the initial 10 unit cell LSMO buffer layer.

Figure 3 shows the RHEED response during growth of the sequence $(\text{LSMO})_3/\text{SrO}/(\text{LSMO})_3$ directly onto the TiO_2 terminated STO (001) substrate. The first $(\text{LSMO})_3$ block was deposited at 850 °C using a laser pulse rate of 3 Hz and was accompanied by clear RHEED oscillations. Superstructure peaks were observed in [110] oriented RHEED patterns taken after the first three unit cell deposition of LSMO (RHEED pattern 2 in Figure 3). These peaks do not correspond to the known polymorphs of LSMO, nor to twinning. They are not present in any RHEED pattern taken after subsequent LSMO layers in the deposition (RHEED images 4,5, Figure 3). The cause of these superstructure peaks is not known, but may be due to a surface reconstruction that occurs in LSMO alone but is inhibited by the layering of LSMO with SrO to form an RP structure. As implied by the RHEED response and STEM/EELS results (Figure 2), after LSMO deposition the surface termination should remain BO_2 as was the case for the pristine substrate. The LSMO layer was annealed for 10 min at the growth temperature to improve the surface, as determined by an increase in the specular RHEED intensity. The substrate

temperature was then reduced to 700 °C: the optimized growth temperature for the RP structure. The first SrO layer was grown onto the BO_2 terminated LSMO at a laser pulse rate of 1 Hz, which resulted in a clear RHEED oscillation. The in-plane lattice parameter of the completed SrO layer derived from the separation between RHEED spots along the $\langle 110 \rangle$ direction (Figure 3) was identical to that of both the starting LSMO surface and the STO substrate, showing that the SrO layer had continued the perovskite structure rather than forming a separate rock salt phase. Such a change in structure from perovskite to rock salt is readily determined by RHEED in this way.⁵² Subsequent growth of three unit cells of LSMO also yielded clear RHEED oscillations. Growth of an integer number of LSMO unit cells onto an AO terminated surface is expected to yield an AO terminated surface, as shown in Figure 3. In this initial growth cycle, the RP structure is not formed; instead, the perovskite structure is continued with the extra SrO layer serving to switch the termination from BO_2 to AO, as shown in Figure 3, and observed by others in similar deposition sequences,⁵³ and as observed here by STEM/EELS (Figure 2). Using the pulse numbers from these initial layers, a second cycle of $\text{SrO}/(\text{LSMO})_3$ was deposited. It is notable that in this second cycle, no RHEED oscillation is seen upon deposition of SrO, but instead a decrease in specular intensity is observed. None of our attempts to optimize the growth conditions could induce a RHEED oscillation during the deposition of SrO atop AO terminated LSMO. This difference in behavior is then likely due to differences in RHEED response upon deposition of SrO on differently terminated perovskite surfaces under these conditions. RHEED oscillations were observed during the subsequent growth of LSMO, which led to recovery of the RHEED intensity close to that prior to the SrO deposition (Figure 3b).

The pulse numbers obtained from RHEED oscillations seen during growth of the first cycles were used to continue the growth up to a thickness of 20–30 unit cells (55–85 nm). To promote growth of SrO in a single 2D layer, which is necessary for structural fidelity of the growing film, the interval deposition technique was used.^{54–56} This involves deposition of the exact amount of material necessary for a single unit cell layer as rapidly as possible and has previously been used in deposition of superlattices by PLD.⁵⁶ The short time interval for growth of the complete layer minimizes multilevel growth. Accordingly, after accurate determination of the correct pulse number for SrO deposition in the first deposited layer, a laser repetition rate of 20 Hz was used for deposition of subsequent SrO layers. Notably, very little RHEED intensity recovery was seen after interval deposition of SrO (this was also the case if instead this SrO deposition was carried out in standard mode at 1 Hz; see Supporting Information Figure S3). A similar RHEED response was observed by Koster et al. in their interval deposition of BaCuO_2 ,⁵⁶ although they associated this with an incorrect pulse number; in our case, the structural properties of our films (vide infra) suggest that the SrO pulse number defined using the method described above is close to optimal. The LSMO layers were deposited using standard mode PLD, at a laser pulse rate of 3 Hz. The use of this mixed interval mode/standard mode deposition technique yielded considerably higher quality films (as assessed by XRD) as compared to standard mode deposition alone (see Supporting Information Figure S3).

The RHEED response during the extended deposition, shown in Figure 3c, is essentially unchanged from that of the second cycle (Figure 3b). RHEED intensity falls during SrO

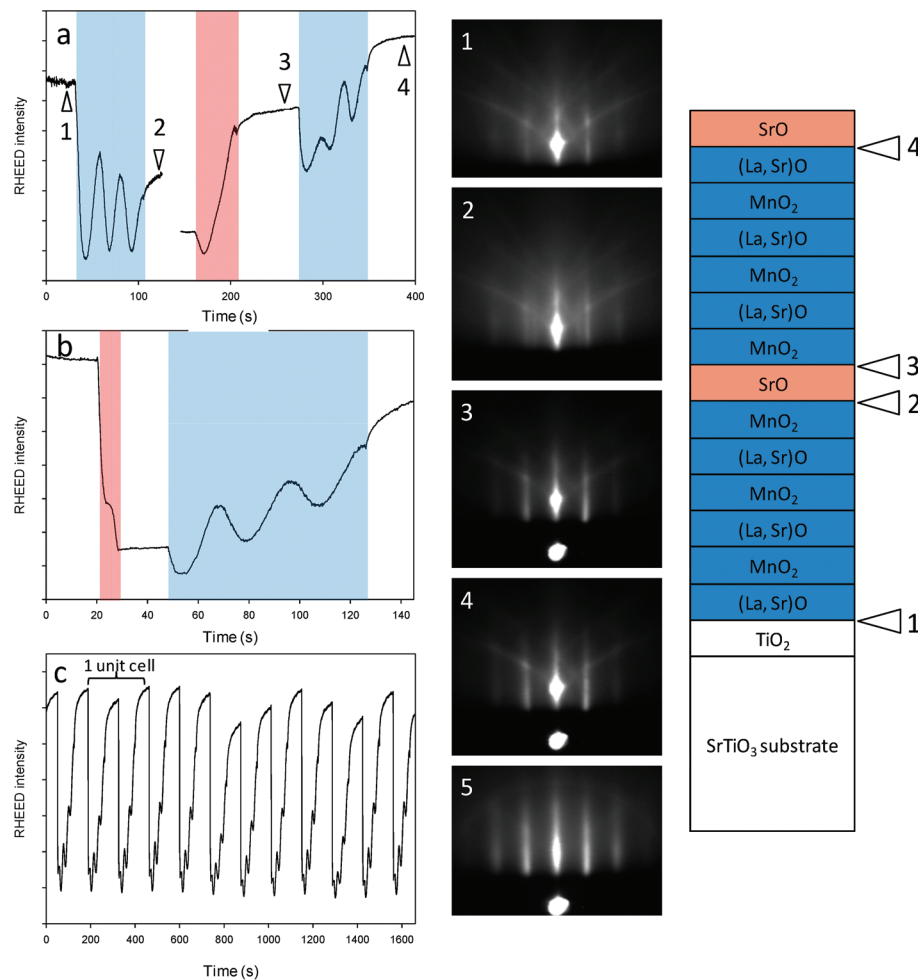


Figure 3. RHEED response upon growth of LSMO (blue shading) and SrO (red shading) components of the $\text{La}_2\text{Sr}_2\text{Mn}_3\text{O}_{10}$ RP3 structure. (a) Standard mode growth of $(\text{LSMO})_3/\text{SrO}/(\text{LSMO})_3$ on a TiO_2 terminated SrTiO_3 substrate. (b) Subsequent interval mode growth of SrO followed by standard mode growth of $(\text{LSMO})_3$. (c) Growth of repeated cycles of $(\text{SrO})(\text{LSMO})_3$. The central column shows RHEED patterns taken along a $\langle 110 \rangle$ direction. Patterns 1–4 were taken at the points indicated in panel (a). RHEED pattern 5 was taken at the end of the deposition. Kikuchi lines are clearly visible in patterns 1–4, and weakly visible in pattern 5. The diagram to the right shows the initial sequence of deposited layers. The numbered arrows correspond to the positions in panel (a) and the numbered RHEED patterns.

deposition and recovers during LSMO deposition. These oscillations persist throughout the duration of the film growth with a reasonably constant overall envelope. The RHEED pattern along the $\langle 110 \rangle$ direction remained streaky, indicating a relatively flat surface.

Gross deviation (>20%) from the required pulse number for SrO or LSMO led to a gradual dampening of the RHEED oscillations during extended film growth. However, smaller deviations from the optimal pulse numbers were tolerated, and RHEED oscillations persisted throughout, although the resulting films did not show the correct RP3 structure by XRD, as described in detail in the following sections. Even in these cases, however, a streaky RHEED pattern resulted at the end of the growth. The SrO/LSMO growth process is therefore relatively robust; both LSMO and SrO could be grown on partially complete layers of the other material without significantly roughening the surface. While this made maintenance of a smooth surface during growth relatively straightforward, it also meant that the persistence of RHEED oscillations or the observation of a streaky RHEED pattern was not a guarantee of growth of the correct structure. It was observed in general that for this system, the presence of

RHEED oscillations and a constant RHEED envelope during growth, and a streaky RHEED pattern at completion of the deposition, were not definitive indicators of formation of the correct structure.

Structural Characterization. A cross section of a RP3 film was analyzed using the high angle annular dark field (HAADF) scanning transmission electron microscopy (STEM) technique. Figure 4a–f shows regions of the film in which the perovskite trilayer structure is clearly visible. In HAADF STEM images, the intensity of the spots is proportional to Z^n ($1 < n < 2$), where Z is the atomic number. Therefore, in Figure 4, the bright spots correspond to the heavier A site cations. There are two different A cation sites in the ideal $I4/mmm$ $n = 3$ Ruddlesden–Popper structure: the 9-coordinate rock-salt (R) site and the 12-coordinate perovskite (P) site. In bulk ceramic samples containing multiple A site ions, the difference in R and P site coordination can drive cation ordering, with the smaller radius cation favoring the lower coordinate R site.⁵⁷ Because La^{3+} is only slightly smaller than Sr^{2+} , this effect is expected to be small for RP structures based on LSMO, but is measurable.⁵⁷ For the deposition technique used here, which is by its nature a far from equilibrium process, different A site orderings might be

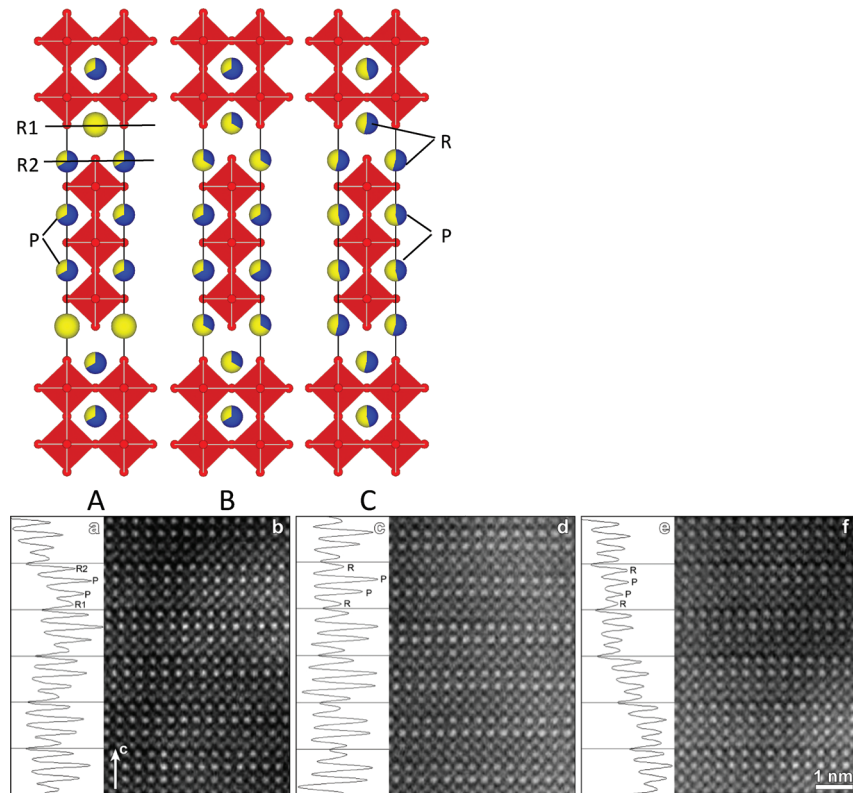


Figure 4. Models of the ideal $\text{La}_2\text{Sr}_2\text{Mn}_3\text{O}_{10}$ RP3 structure with different A site orderings; the A site cations are colored (La blue, Sr yellow) according to their occupancy: (A) The as-deposited structure with pure SrO rock salt layer. In this structure, the R sites may be split into R1 and R2, as described in the text. (B) The mixed R site structure. (C) The structure with disorder of La and Sr over both sites. (a–f) Cross-sectional HAADF TEM micrograph of an RP3 film grown at 2 mTorr. Bright spots in (a),(d),(f) represent A site cations. (a),(c),(e) are plots of image gray scale value against distance in the growth direction calculated from the TEM images shown. Vertical lines represent half unit cell distances; the positions of the P and R sites are shown in one such division. The P sites in (a) and (c) have greater HAADF image intensity, corresponding to greater mean atomic number and showing that the P sites are La rich and the R sites are Sr rich, with further distinction between the R1 and R2 sites as in model A apparent in (a). This ordering is contrary to the thermodynamically stable arrangement and shows the as-deposited ordering is partially kinetically trapped.

expected. In the deposition sequence used to synthesize RP3 samples, three perovskite blocks, with A site stoichiometry $\text{La}_{0.67}\text{Sr}_{0.33}$, are deposited followed by a rock salt layer with only Sr on the A site. In this “as-deposited” structure, there are now two distinct R sites (labeled R1, R2 in Figure 4, model A), one with $\text{La}_{0.67}\text{Sr}_{0.33}$ on the A site and one with only Sr. In a second conceivable A site arrangement (Figure 4, model B), the cations in neighboring rock salt layers might mix, resulting in a Sr-rich composition ($\text{Sr}_{0.67}\text{La}_{0.33}$) on the R sites and a La-rich composition ($\text{La}_{0.67}\text{Sr}_{0.33}$) on the P sites. This is the “mixed R site” structure. Figure 4, model C, shows a random distribution of Sr and La over both R and P sites. Figure 4a–f also shows three HAADF-STEM images of different areas of the film, showing correspondence to the different models.

A plot of image intensity against distance in the growth direction, shown in Figure 4a–f next to each experimental image, reveals peaks corresponding to the A site positions. Peaks arising from the different A sites can be distinguished by their peak separation; the R–R distance is smaller than the P–P distance due to its intervening MnO_2 layer. The HAADF pixel intensity plot reveals a difference in the occupation of the P and R sites. Figure 4a shows a region that resembles the contrast expected for the “as-deposited” ordering, that is, an R1 layer made up entirely of Sr, therefore showing low HAADF intensity, and the R2 and P layers predominantly composed of La, and showing higher and equal HAADF intensity. In the

region shown in Figure 4c,d, the P sites generally have higher pixel intensity as compared to the R sites, suggesting that the P sites are more La rich. Neighboring R peaks have similar intensity, suggesting little or no difference in the occupation of the R1 and R2 sites and thus more extensive mixing between the initially LSMO- and AO-derived rock salt layers. However, in other areas of the film (Figure 4e,f), this distinction between P and R sites is almost absent, and all A sites appear with similar HAADF image intensity. Therefore, it appears from the TEM analysis that some areas of the film show A site ordering, with the R sites being Sr rich and the P sites La rich, while other areas show no such ordering. The observed “mixed R site” and “as-deposited” orderings, where present, are contrary to the expected equilibrium cation ordering; the smaller A cation, La^{3+} , is found predominantly on the higher coordinate P sites in ordered regions of our samples, rather than on the lower coordinate R sites as expected. Therefore, it seems that the unstable ordering is formed due to the mode of deposition, specifically the deposition of rock salt layers containing only Sr on the A site, while the perovskite blocks are deposited with A site composition $\text{La}_{0.67}\text{Sr}_{0.33}$. The observed cation ordering, either as-deposited or where the R1 and R2 sites are compositionally mixed, but the P and R site composition is appreciably different from the expected equilibrium values, is likely then a result of only limited A cation mobility at the deposition temperature. The A cations can exchange between

neighboring R layers, but exchange between R and P layers is more limited.

The relative stability of different A site orderings was examined using DFT. The “as-deposited” and “mixed R site” models shown in Figure 4 were modeled using the supercells shown in Figure 5. The DFT results are in agreement with the

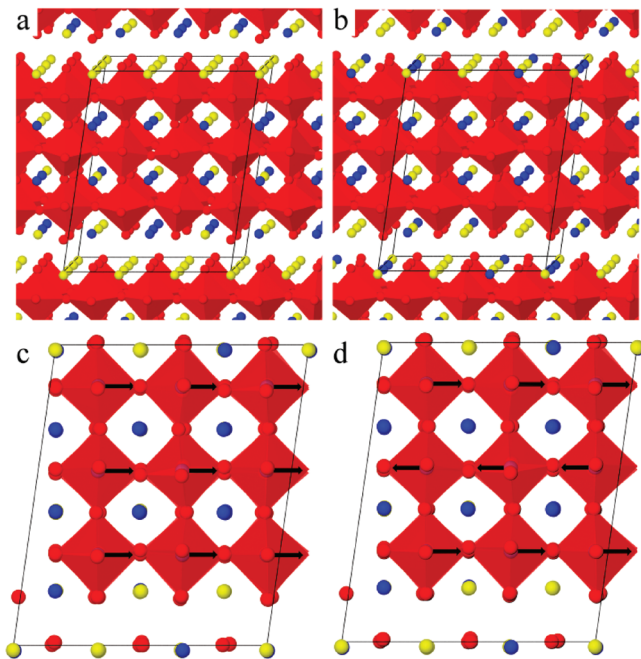


Figure 5. Structural diagrams of two representative supercells used in the DFT calculations for the $\text{La}_2\text{Sr}_2\text{Mn}_3\text{O}_{10}$ RP3 films, with the (a) “as-deposited” and (b) “mixed R site” layer compositions for the rock-salt layers. (La blue, Sr yellow) Also shown are diagrams of the (c) ferromagnetic and (d) A-type antiferromagnetic orderings used in the DFT calculations, with the magnetic moments on the Mn cations represented as black arrows.

experimentally observed A site ordering. The formation energy of the five “mixed R site” structures, calculated relative to LSMO and SrO, is -0.29 ± 0.02 eV/formula unit (FU), showing that the RP3 phase is calculated to be more stable than LSMO and SrO. The corresponding formation energy of the five “as-deposited” structures is -0.26 ± 0.03 eV/FU. The “mixed R site” structures are more stable than the “as-deposited” structures with a pure SrO layer, suggesting that mixing of the R1 and R2 sites should occur, as seen in experiment. Furthermore, R sites in the mixed structures are Sr rich with composition $\text{La}_{0.33}\text{Sr}_{0.67}$ and the P sites are La rich with composition $\text{La}_{0.67}\text{Sr}_{0.33}$, consistent with the ordering observed from the TEM analysis. The desired cation ratios are readily accommodated within the 3×3 supercells. Tabulated Mn–O bond lengths can be found in the Supporting Information, Table S1.

Symmetrical $\theta/2\theta$ XRD scans showed peaks that were indexed to the $(00l)$, with $l = \text{even}$, reflections of the tetragonal RP3 phase, with additional peaks due to the SrTiO_3 substrate. For the RP3 film shown in Figure 6a, all expected peaks up to (0020) are present. Bragg peak intensities were simulated in FullProf using the as-deposited, mixed R site, and random arrangements of A cations (these structures are shown in Figure 4). The simulated results are shown in Figure 6a; according to these, the various A site orderings cause only small changes in

the expected $(00l)$ diffracted intensities, and it was found that each arrangement, including the mixed R site arrangement implied by TEM, matches well to the experimental sequence. However, notably in films where there was a slight deviation from the correct pulse numbers for growth of the LSMO or SrO layers, the expected $(00l)$ intensities were not observed, most notably in the (002) peak, which was typically much reduced in intensity. Gross deviations from the correct pulse numbers resulted in an absence of all but the intense (008) and (0014) reflections, and as such the correct sequence of diffracted intensities appears to be a sensitive test for formation of the correct structure. Examples of diffraction patterns from defective films are shown in the Supporting Information (Figure S3). Bulk Ruddlesden–Popper phases display a range of defects,⁵⁸ and the films that do display RP3 diffraction patterns with correct intensities also contain defects corresponding to higher n (Figure S4), and steps parallel to the substrate–film interface (Figure S5). These steps can occur along both directions a and b , with a relative shift of the unit cells along the c -direction.

Varying the growth pressure from 0.7 to 10 mTorr led to changes in the out-of-plane lattice parameter, c , from 28.38 to 27.88 Å, as shown in Figure 6b. Where cation composition and structure allow, as it does in this case, oxide films grown at low pressure are commonly oxygen deficient. Oxygen over- or under-stoichiometry in perovskite manganites has a strong influence on magnetic properties because it alters the Mn charge state.⁴³ It has been shown that changes in lattice parameters are often a poor measure of oxygen stoichiometry in perovskite oxides, because assumptions of precise cation stoichiometry are often unfounded.⁵⁹ However, in bulk and thin film LSMO, there is convincing evidence that oxygen deficiency leads to a larger lattice parameter as compared to the stoichiometric compound, due to an increase in ionic radius of the Mn cations.^{43,60–62} Considering the careful optimization of the PLD process to yield cation stoichiometric growth, we therefore interpret the observed decrease in lattice parameter of the RP3 films with increasing growth pressure as indicative of increasing oxygen content in the films. The structural parameters of the RP3 phase have not previously been reported, but simple linear extrapolation from the c parameters of the analogous RP1 ($c = 12.48$ Å) and RP2 ($c = 20.14$ Å) phases yields a predicted RP3 c value of 27.80 Å for the bulk phase.^{63–65} The calculated c parameters of RP3 using DFT were 27.79 ± 0.03 Å for the “as-deposited” structure and 27.78 ± 0.02 Å for the “mixed R site” structure. The observed film lattice parameter for the sample grown under 10 mTorr O₂, which was 27.88 Å, is therefore very close to the extrapolated and calculated values. Given that the epitaxial strain is low in this system (+0.77%), the lattice parameters for a fully oxygen stoichiometric film would be expected to correspond closely to the bulk. While the comparison between predicted bulk and observed thin film lattice parameter suggests that the films grown at 10 mTorr are close to stoichiometric in oxygen, it also implies that the films grown at lower pressures were significantly oxygen deficient. Consistent with this, cross-sectional STEM EELS, carried out on the film grown at 2 mTorr, showed a variation in Mn charge state throughout the thickness of the film, suggesting oxygen deficiency because the cation stoichiometry was not found to change. Furthermore, post deposition annealing of films at 600 °C in 1 bar of oxygen led to a reduction in lattice parameter in films grown at lower pressure (0.7–2.0 mTorr), suggesting they were oxidized, but

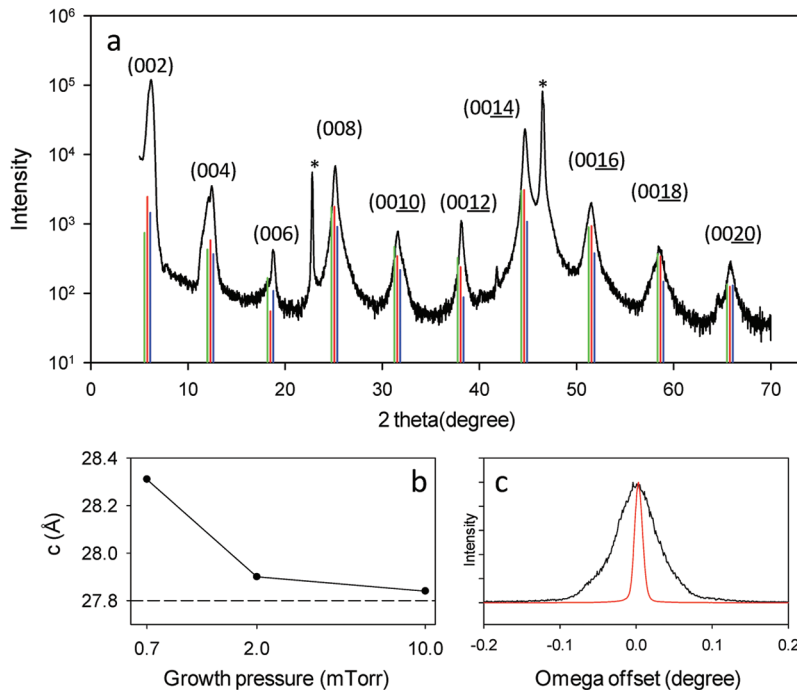


Figure 6. (a) XRD pattern from an $\text{La}_2\text{Sr}_2\text{Mn}_3\text{O}_{10}$ RP3 film on an SrTiO_3 (001) substrate. Vertical bars show the intensity of simulated RP3 (001) $I4/mmm$ diffraction peaks using the as-deposited (green) mixed R site (red) and random (blue) arrangements (see text and Figure 4 for description of these arrangements). Asterisks mark diffraction from the substrate (b) change in lattice parameter c with varying growth pressure. The dashed line represents the value expected from simple extrapolation based on the $n = 1$ and $n = 2$ members of the series (c) ω -scan (rocking curves) taken around the RP3 (0014) peak (black) and STO (002) peak (red).

no such lattice parameter change was observed in the film grown at 10 mTorr, again suggesting that it is close to full oxygenation. Omega scans centered on the RP3 (0014) peak and the SrTiO_3 (002) peak were carried out along low symmetry in plane directions, and showed peaks with FWHM's of 0.067° and 0.012° , respectively, with peak maxima at identical omega offset values, showing that film and substrate were closely aligned (Figure 6c). Broadening of the base of the peak in the omega scan taken from the film indicates a degree of twinning in the films, which was found in high-resolution scans (not shown) to mirror that seen in the substrate. Alternatively, such broadening may indicate a degree of mosaicism present in the film independently of the substrate.⁶⁶ Off axis diffraction peaks were measured using reciprocal space maps (RSM). The RSM of the RP3 film recorded around the SrTiO_3 (013) peak is shown in Figure 7. Peaks originating from the film are indexed as the (0121) and (0123) peaks of the RP3 phase. In the high-resolution scans, an elongated shape to these films peaks is further evidence of a somewhat mosaic like structure.^{67,68} From the centroid of these peaks, the in-plane RP3 lattice parameter was determined to be $a = 3.91 \text{ \AA}$, very close to that of the SrTiO_3 substrate (3.905 \AA). This suggests that the film remains strained to the substrate throughout its thickness (70 nm), which is not unexpected for an epitaxial film with a comparatively low mismatch (+0.77%). The alignment of the off axis film and substrate peaks along the $\langle 001 \rangle$ direction indicates there is no measurable tilt between the film and the substrate. Notably, no perovskite peaks nor other RP phases are detected in any diffraction pattern, either symmetrical scan or reciprocal space map. The observed c/a ratio of 7.25 is close to that found for bulk $\text{Ca}_4\text{Mn}_3\text{O}_{10}$ (7.22),⁶⁹ which itself lies within the range usually found for bulk $n = 3$ RP materials.

Magnetism. Figure 8 shows the temperature dependence of the magnetic susceptibility, measured in the magnetic field $H = 1 \text{ kOe}$ during warming after cooling in zero-field (ZFC, ○) or during cooling in the same field (FC, ●) from 300 to 5 K. The magnetic field was applied in the ab plane (in-plane, Figure 8a) or in the c direction (out-of-plane, Figure 8b). The in-plane ZFC curve increases as the temperature is lowered and then starts to decrease at temperatures below 34 K, showing a cusp. In comparison, the in-plane FC curve does not have a strong anomaly at 34 K, but shows a kink at temperatures below 34 K. In contrast, the out-of-plane ZFC curve is rather flat below 34 K with a smeared cusp around 20 K, and the out-of-plane FC curve starts to deviate in the same temperature interval. The comparison between the in-plane and the out-of-plane curves demonstrates the magnetic in-plane anisotropy of the film. Further, we can see a magnetic freezing process taking place below $T_C = 34 \text{ K}$. By comparison with the results for the $n = 1$ member of Moritomo et al.,⁶⁵ these findings can be interpreted in terms of a spin glass (SG)-like ground state. Note that the measured susceptibility for our samples has the same order of magnitude as in the case $n = 1$ with $x = 0.3$,⁶⁵ while the corresponding freezing temperature is higher (34 K for $n = 3$ here vs 16 K for $n = 1$).

To prove this hypothesis, we performed a memory effect test⁷⁰ by measuring ZFC magnetic moment m versus T curves during warming from 5 to 65 K in the applied in-plane magnetic field $H = 1 \text{ kOe}$ after cooling the sample in zero-field from 300 to 5 K in two different cooling protocols. In the first protocol, the cooling process has been interrupted for an intermittent stop at the waiting temperature, $5 \text{ K} < T_{\text{wait}} < 65 \text{ K}$. The cooling was then resumed after a waiting time, t_{wait} , to measure m . In the second protocol, the sample was cooled in zero-field without any interruptions, to measure the reference

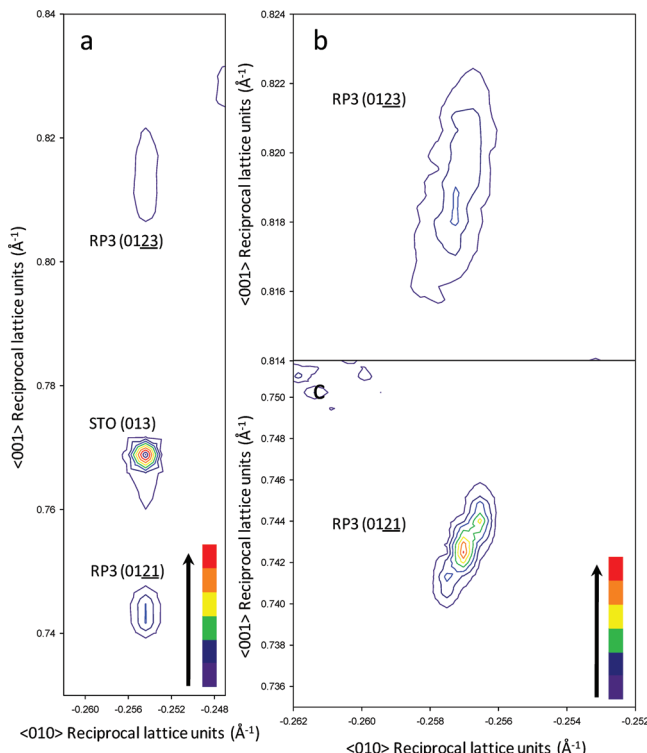


Figure 7. Reciprocal space maps of $\text{La}_2\text{Sr}_2\text{Mn}_3\text{O}_{10}$ RP3 film grown at 0.7 mTorr around the STO substrate (013) peak. (a) Wide angle, low-resolution scan showing substrate and two RP3 peaks with gradients plotted on a log scale for ease of comparison (color key in bottom right corner). The peaks are collinear along (010) showing a high degree of alignment between film and substrate. High-resolution scans around RP3 (0123) and (0121) are shown in (b) and (c), respectively, with gradient lines plotted on a linear scale; each contour represents 50 count/s. The elongated shapes are indicative of a degree of mosaicism in the films.

curve m_{ref} for the first cooling protocol. By plotting both curves together, as in Figure 9, a dip becomes visible in the vicinity of $T_{\text{wait}} < 34$ K. It has its origin in the magnetic state “aging” during the waiting time t_{wait} . In parallel, no difference is observed for the waiting temperature $T_{\text{wait}} = 40$ K, which is above 34 K. This proves a magnetic state relaxation below $T_g = 34$ K. Note that a comparable relaxation of a ferromagnetic domain state would result in a “global” decrease for the whole temperature interval below T_{wait} . In contrast to that, we observe here another characteristic feature of the SG state, the so-called rejuvenation,⁷¹ as shown by the recovery of the ZFC curve after the waiting, if measured at temperatures, which are far enough from T_{wait} . Both effects can also be seen in the temperature dependence of the difference $m_{\text{ref}} - m$, showing the characteristic “hole” in the vicinity of T_{wait} . Thus, the measurements of the magnetic memory effect prove that the magnetic state below 34 K can be interpreted as a SG-like state.

In addition, we measured thermoremanent magnetization (TRM) during slow warming at rates 1 K/min from 5 K after cooling in the 30 kOe field from 300 to 5 K (Figure 10a). With increasing temperature, we observe first a rapid decay of the TRM values until $T \approx 34$ K, followed by a gradual approach to zero up to 150 K. The moment remaining at higher temperatures can be assigned to magnetic impurities within the SrTiO_3 substrate. For discussion of the temperature interval $34 \text{ K} < T < 150 \text{ K}$, see below. In Figure 10b, the slow TRM relaxation versus time at $T = 24$ K is shown after cooling to 24 K in the field $H_{\text{fr}} = 1$ kOe, and removing the field after 120 s waiting time. In contrast, no relaxation was observed at $T = 40$ K in a TRM versus time measurement under the same conditions, in agreement with results of the memory effect test (Figure 9). More clearly, the relaxation is illustrated by fits to the stretched exponential decay, $m = m_0 \exp[-(t/\tau)^{\beta}]$, which is often encountered in glassy systems.⁷² The fitting yields exponent values $\beta = 0.357 \pm 0.096$ and 0.005 ± 0.055 at $T = 24$ and 40 K, respectively, with the exponent $\beta = 0.357$ being close to the typical SG values,⁷³ and that above the freezing temperature being zero within error.

The relatively small volume of material in thin film samples makes detailed analysis of relaxation and ac-dynamics by means of SQUID magnetometry a challenging problem, which still needs to be solved. Without these sorts of tests, we cannot reach a definitive conclusion about the nature of the observed low- T glassy state. A comparison with another spin glass system, $\text{La}_{1-x}\text{Sr}_x\text{CoO}_3$,⁷⁴ leads us to an assumption of a “pure” atomic, not cluster, SG in the case of our RP3 phase, because of the relatively sharp cusp form in the ZFC curve (Figure 8a) and due to the reduced glass freezing temperature of 34 K. However, given the nature of the samples, this cannot be a definitive assignment.

The idea of the SG-like state is supported by the magnetic hysteresis loops, measured in the in-plane geometry at temperatures below and above the freezing temperature, 34 K (Figure 11). We see no magnetic saturation up to the maximum field of 6 T. Both branches of the hysteresis loop at 5 K coincide with each other at fields above 30 kOe. In combination with the reduced magnetic moment of about $0.6 \mu_B$ per Mn ion at 60 kOe, this indicates the presence of frustrated AF and FM interactions. A nonlinear magnetic field dependence as seen at $T = 75$ K might be explained by a small fraction of homogeneous long-range ferromagnetic order coexisting in the film. In fact, careful examination of Figure 8 reveals small deviations between the ZFC and FC curves for both field

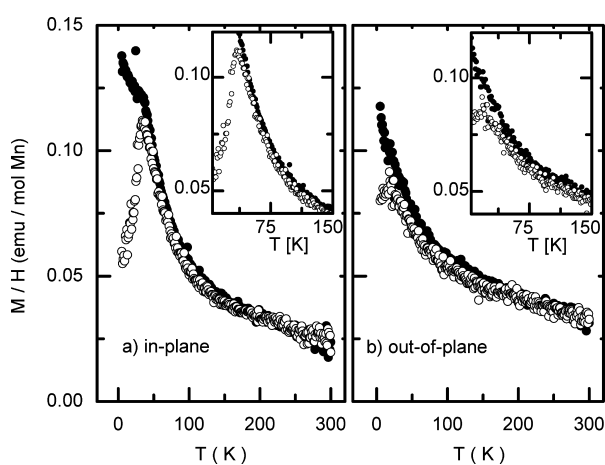


Figure 8. Temperature dependence of magnetic susceptibility M/H for thin film $\text{La}_2\text{Sr}_2\text{Mn}_3\text{O}_{10}$ (insets: low-temperature data magnified), measured during warming in the magnetic field $H = 1$ kOe after zero-field cooling from 300 to 5 K (○) or during cooling in the field from 300 to 5 K (●). Magnetic field was applied parallel (a) or perpendicular (b) to the layer plane ab , respectively. Diamagnetic background signal of the SrTiO_3 (001) single crystal substrate has been subtracted from the raw data.

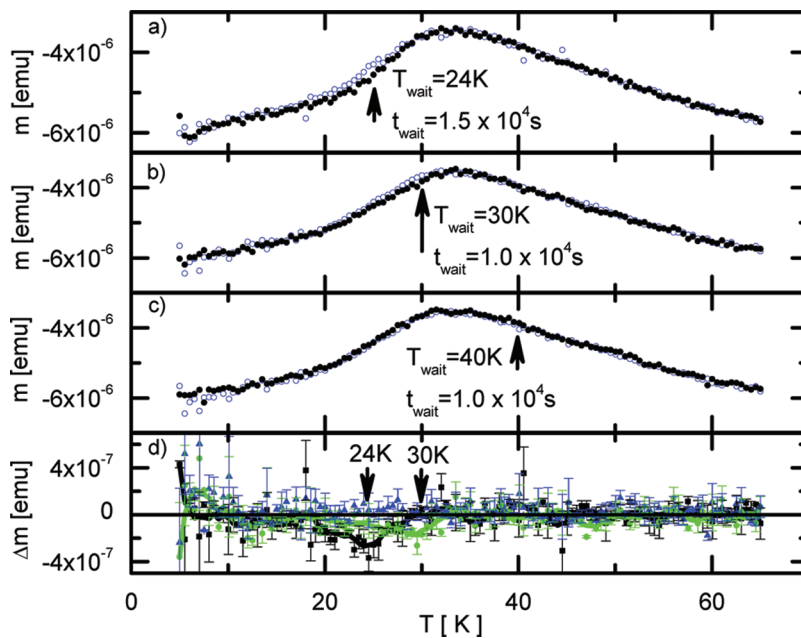


Figure 9. (a–c) Magnetic moment, m , versus temperature, T , measured on $\text{La}_2\text{Sr}_2\text{Mn}_3\text{O}_{10}/\text{SrTiO}_3$ (001) in applied magnetic field, $H = 1$ kOe, parallel to the layer plane ab . Measurements were performed during warming from 5 to 65 K after zero-field cooling from 300 to 5 K with (●) and without (reference curve, ○) intermittent stop at waiting temperature $T_{\text{wait}} = 24$ K (a), 30 K (b), and 40 K (c) with the corresponding waiting times $t_{\text{wait}} = 1.5 \times 10^4$ s (a) or 1.0×10^4 s (b,c), respectively. (d) Difference $\Delta m = m - m_{\text{ref}}$ versus temperature T , calculated between the curves, m , measured after waiting at $T_{\text{wait}} = 24$ K (■), 30 K (green ●), and 40 K (blue ▲) and the reference curve, m_{ref} , respectively. Lines correspond to averaging between five adjacent values in the cases of $T_w = 24$ K (black) and $T_w = 30$ K (green). The positions of the dip holes are indicated by arrows.

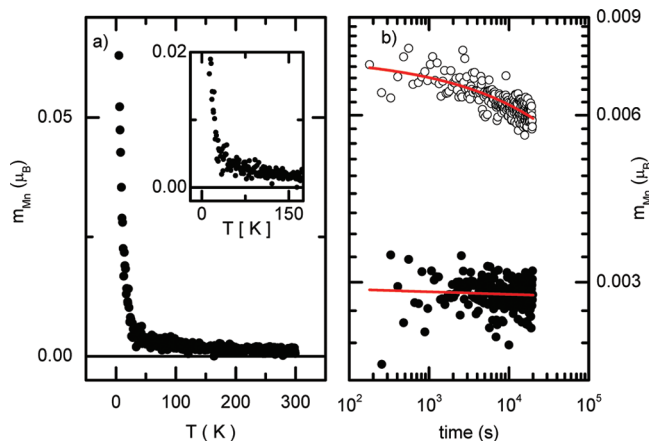


Figure 10. (a) Temperature dependence of thermoremanent magnetization (TRM) per Mn ion, m_{Mn} , for thin film $\text{La}_2\text{Sr}_2\text{Mn}_3\text{O}_{10}$ (RP3), measured during warming after field cooling in $H = 30$ kOe from 300 to 5 K. Inset: Low-temperature data magnified. (b) Time dependence of TRM, measured after field cooling in $H = 1$ kOe from 300 to 24 K (○) and to 40 K (●), respectively. Magnetic field was applied parallel to the layer plane ab . Solid lines present best fits to the stretched exponential decay $m = m_0 \exp[-(t/\tau)^{\beta}]$.

orientations at temperatures above 34 K up to 150 K. It could also have its origin in magnetic spin correlations in a paramagnetic regime, which have been observed before in layered $n = 2$ RP phases⁶² and 2D ferromagnets.⁷⁵

A comparison of the temperature dependences of the magnetization in 1 kOe (Figure 8) and 10 kOe (Figure 12) for both sample orientations shows the disappearance of the cusp in the ZFC curve for the out-of-plane orientation in the higher field. In the in-plane geometry at $H_{\text{fr}} = 10$ kOe, one can

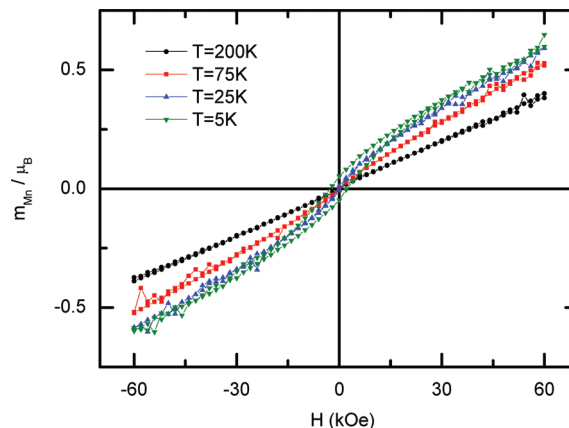


Figure 11. Magnetic moment per Mn ion, m_{Mn} , versus applied magnetic field, H , measured at different temperatures with the field parallel to the layer plane ab . The solid lines are guides to the eye. Diamagnetic background signal of the SrTiO_3 substrate, $-0.0329 \mu_{\text{B}}/\text{kOe}$, has been subtracted from the raw data, as obtained from the corresponding hysteresis loop measurements on a SrTiO_3 (001) single crystal.

still observe a cusp corresponding to magnetic freezing, although at a lower temperature of 28 K. A similar picture is observed for the comparison between the in-plane and out-of-plane orientations in Figure 8. This interesting finding proves the in-plane character of the magnetic frustration, which is responsible for the SG-like state. Similar examples can be found in the Ising-type spin glasses Fe_2TiO_5 and $\text{Fe}_{0.5}\text{Ti}_{0.5}\text{MnO}_3$.^{76,77} The in-plane and out-of-plane anisotropy becomes clearly distinguishable at temperatures below 150 K (as compared to 370 K for the corresponding bulk single crystal $n = 2$ phase and 300 K for $n = 1$),⁶² which is significantly above the freezing

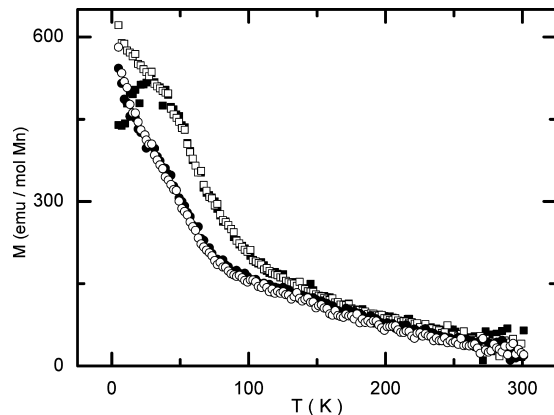


Figure 12. Temperature dependence of magnetization M for thin film $\text{La}_2\text{Sr}_2\text{Mn}_3\text{O}_{10}$, measured during warming in magnetic fields, $H = 10$ kOe, from 5 to 300 K. Measurements were performed on warming after zero-field cooling (filled symbols) or after field cooling (open symbols) in the field $H_{\text{fr}} = 10$ kOe from 300 to 5 K, with the magnetic field applied parallel (squares) or perpendicular (circles) to the film plane ab . Diamagnetic background signal of the SrTiO_3 (001) single crystal substrate has been subtracted from the raw data.

temperature of the SG-like state. Apparently, anisotropic exchange interactions in combination with spin fluctuations are responsible for this effect.

Consistent with the structural response to growth in different pO_2 and postsynthesis annealing, there is no significant change in the magnetic behavior on postdeposition annealing in O_2 , and additionally the same magnetic features were observed in different samples prepared in the same fashion.

DFT calculations of ferromagnetically ordered RP3 give a mean magnetic moment of $3.33 \mu_B$ on the Mn atoms. We also performed calculations for one of the “as-deposited” and one of the “mixed R site” structures of RP3 with A-AF ordering, as is found for some $n = 2$ compositions and is predicted for the related RP series $\text{La}_{3-3x}\text{Ca}_{1+3x}\text{Mn}_3\text{O}_{10}$.⁷⁸ The spins within each MnO_2 layer were FM aligned, and each layer within the perovskite block was AF aligned with its neighbors. Layers were FM aligned across the rock salt layers. The FM and A-AF structures are shown in Figure 5. For both A site orderings, the c parameter was reduced to 27.64 \AA upon imposition of A-AF ordering, which was found to be 0.02 eV/FU less stable than the FM ordering. The mean magnetic moment was reduced to $1.11 \mu_B/\text{Mn atom}$, one-third that of the FM ordering, as expected. The relative instability and reduced c parameter of the A-AF ordering suggest that this is not the ground-state magnetic ordering for RP3, although we note that the energy difference as compared to FM ordering is small.

Transport Properties. Temperature dependence of in-plane resistivity, ρ_{ab} , shows insulating or semiconducting behavior with no indication of any phase transitions between 100 and 360 K (Figure 13). This behavior is consistent with our conclusions of a SG-like magnetic ground state. Qualitatively, the resistivity curve of RP3 has strong similarity with that of the $x = 0.3$ RP1 phase (which also has a SG-like ground state) and is different from the RP2 phase, which shows a phase transition close to the FM T_C .^{16,24,62,65} The room temperature resistivity of RP3 is within an order of magnitude of single crystal RP1 and RP2 samples of similar composition. At low temperature, the order of in-plane resistivity is RP1 > RP3 > RP2, with differences of more than an order of magnitude in each case. That RP3 shows lower in-plane resistivity than RP1 might be

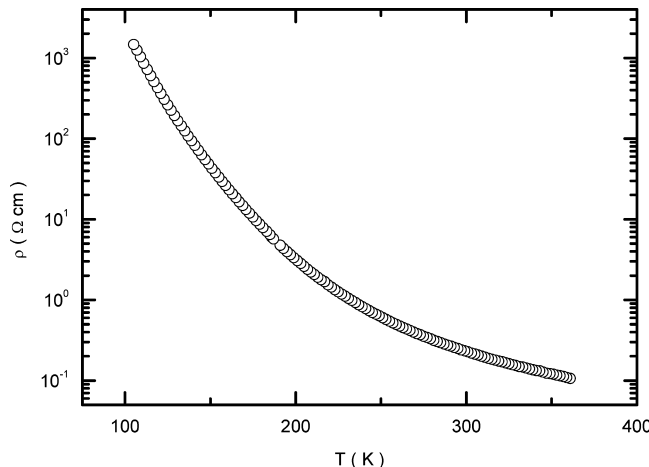


Figure 13. Temperature dependence of in-plane resistivity ρ for thin film $\text{La}_2\text{Sr}_2\text{Mn}_3\text{O}_{10}$, measured during cooling.

expected given that RP3 has thicker conducting perovskite blocks. The still lower resistivity of RP2 can be explained by its transition to a metallic FM state at low temperatures.^{62,65}

■ DISCUSSION

Substrate Strain versus Growth Kinetics. Despite intense interest in the layered perovskite manganites, very few examples of $n = 3$ Ruddlesden–Popper manganites have been studied. The pure Mn^{4+} $n = 3$ RP phase $\text{Ca}_4\text{Mn}_3\text{O}_{10}$ has been produced in bulk form; the Sr and Ba analogues form a distinct orthorhombic structure with corrugated layers of linked Mn_2O_{12} units.^{69,79–85} Synthesis of phase pure A site doped mixed valence $n = 3$ phases is more problematic; the stability of the $n = 3$ structure for Ca leads to limited La doping (up to 10%) of bulk $\text{Ca}_4\text{Mn}_3\text{O}_{10}$, although this was not enough to significantly change the magnetic ground state,⁸⁶ and more heavily doped $n = 3$ $\text{La}_{2.1}\text{Ca}_{1.9}\text{Mn}_3\text{O}_{13}$ with the unusual $c/a = 6.9$ and a ferromagnetic ground state accessible as strained films on MgO .⁸⁵ It has not so far proved possible to access and magnetically characterize $n = 3$ phases in the RP series derived from the archetypal colossal magnetoresistive oxide LSMO. Moritomo et al. were unable to produce single crystals of $(\text{SrO})(\text{LSMO})_3$.⁶² High pressure synthesis has been attempted, but yielded a mixture of products.^{87,88} Bulk synthesis of two $(\text{SrO})(\text{LSMO})_3$ phases was reported, but no details of structural parameters or phase purity were given.^{64,89} An alternative to A site doping is electron doping of $\text{Ca}_4\text{Mn}_3\text{O}_{10}$ by introduction of pentavalent ions onto the B site, which has successfully introduced ferromagnetism into these compounds, although B site substitution will naturally have an additional effect on the magnetic interactions.^{90,91} It appears that it is very challenging to produce phase pure samples of $n = 3$ manganite phases in general, and $(\text{SrO})(\text{LSMO})_3$ in particular through standard bulk synthesis methods. Furthermore, our attempts at ceramic synthesis of the RP3 composition studied here failed to yield the desired product. As presented earlier, DFT calculations showed that RP3 is predicted to be 0.3 eV/FU more stable than stoichiometric amounts of SrO and LSMO, initially suggesting that it should be possible to synthesize RP3 by conventional solid-state methods. However, the energetics of the calculated RP3 structures suggest that RP3 is roughly as stable as a combination of RP2 and LSMO. If the energy of the “mixed R site” layer structures of RP3 are compared to

stoichiometric amounts of RP2 and LSMO, RP3 is found to be only 0.07 ± 0.02 eV/FU more stable than phase separated RP2 and LSMO. A similar treatment of the “as-deposited” structures finds that RP3 is 0.12 ± 0.03 eV/FU less stable than RP2 and LSMO. Given the similar stabilities of the oxides, it is likely that attempts to synthesize RP3 using conventional bulk methods are hindered by the competitive formation of RP2 and LSMO.

Two potential driving forces for the stabilization of thin films of RP3 are substrate-induced strain and kinetic trapping of the structure. The thin films are grown epitaxially on a STO substrate with a slight lattice mismatch. The induced strain is seen to propagate throughout the whole thin film and could result in stabilizing RP3 with respect to RP2 and LSMO. To investigate this possibility, we carried out calculations on one “as-deposited” and one “mixed” structure of RP3 in which the *a* and *b* lattice parameters were allowed to relax, rather than fixing them to the calculated value of STO (3.94 Å). The results were the same in each case. As expected, relaxation of RP3 resulted in a decrease of the calculated in-plane RP3 lattice parameters from 3.94 to 3.91 Å, representing a lattice mismatch of +0.8% between relaxed RP3 and STO, very close to the observed value of +0.77%. There was a corresponding increase in the *c* lattice parameter from 27.8 to 27.9 Å upon relaxation. The fully relaxed structures were only 0.02 eV/FU more stable than the strained structures. It seems unlikely that an energy shift on this scale would be sufficient to dramatically stabilize RP3 relative to RP2, suggesting that strain does not play a significant role in driving RP3 synthesis. Instead, it seems likely that RP3 synthesis in the LSMO system here is the result of kinetic trapping, with the deposition of three LSMO layers on SrO initially forming the RP3, which is unable to phase separate into RP2 and LSMO under the synthesis conditions.

Magnetism. Mixed valence perovskite manganites are model systems for the study of competing magnetic interactions that occur with varying d orbital occupation. In the layered Ruddlesden–Popper manganites, the magnetic perovskite layers are separated by a nonmagnetic layer in the *ab* plane, and this reduced dimensionality introduces yet greater variation in ground-state magnetic properties. In the series $\text{La}_{(n-nx)}\text{Sr}_{(1-nx)}\text{Mn}_n\text{O}_{3n+1}$, the $n = 1$ and $n = 2$ members have been extensively characterized.^{14–21} For the $n = 1$ structure, no long-range ferromagnetic (FM) ordering is observed at any composition, *x*, attributed to reduced influence of the FM double exchange interaction due to greater electron localization in the single perovskite layer.^{21,64,65} The *x* = 0 compound, containing only Mn³⁺, is antiferromagnetically (AF) ordered, with moments ordered parallel to the *c* axis and a Neel temperature (T_N) of around 128 K.^{18,21,92} Magnetic frustration induced by the increasing prevalence of FM exchange interactions causes T_N to decrease with increasing *x*, vanishing between *x* = 0.1 and 0.2, signifying loss of long-range magnetic order.^{18,93} From *x* = 0.2 to around 0.5, a glassy state with no long-range magnetic order exists due to competition between the energetically similar AF and FM exchange mechanisms.⁶⁵ Above *x* = 0.5, AF order re-emerges,^{92,93} possibly with moments orientated in the *ab* plane.¹⁸ There is greater variation in magnetic ground state in the $n = 2$ compounds, although some trends are comparable to those seen for $n = 1$.^{14–17,19,20,22} Below *x* = 0.3, intrablock FM ordering, with moments ordered parallel to the *c* axis, occurs accompanied by interblock AF interactions, yielding a net AF ground state with zero overall moment. Increasing *x* yields FM ordering from *x* = 0.3–0.5, initially ordered parallel to the *c* axis (up to *x* = 0.32,

where T_C is at a maximum) before switching to the *ab* plane, this transition being driven by changes in population of the e_g orbitals caused by lessening Jahn–Teller distortion with increasing *x*.⁹⁴ Increasing *x* above 0.5 yields first A-type AF ordering, with spins aligned FM within each *ab* plane, and across rock salt layers, but AF between perovskite layers. Because *n* is even, this arrangement nominally yields a net zero moment. No long-range magnetic order exists in the composition interval $0.66 < x < 0.74$, and at higher *x*, first C-type then G-type AF order is seen.

We observe a glassy magnetic state in our RP3 samples, which have *x* = 0.33. In our samples, the distribution of A site cations within the structure may provide the criterion of randomness, while competition between FM Mn³⁺–Mn⁴⁺ and AF Mn³⁺–Mn³⁺, Mn⁴⁺–Mn⁴⁺ interactions could be responsible for the magnetic frustration. These factors are known to cause the glassy state in the case of the *n* = 1 RP phase as described above.¹⁸ This is in contrast with the *n* = 2 phase, for which the *x* = 0.33 member has a FM ground state.²² Indeed, if the arguments presented above for the prevalence of AF order in the *n* = 1 compounds, that is, reduced dimensionality of the perovskite block leading to electron localization, are accepted, it would follow that the *n* = 2, 3, and higher materials would have decreasing localization and enhanced FM exchange, favoring more strongly FM ordering and eventually tending to the properties of the perovskite (*n* = ∞), which at *x* = 0.33 is FM ordered above room temperature. While the *n* = 2 member follows this trend, our results suggest that such arguments do not hold for *n* = 3. To explore this observation, DFT was used to calculate magnetic ground states for the various possible A site orderings; however, modeling of SG order by DFT calculations is a relatively complicated task, as the defining characteristics, disorder and magnetic frustration, are not straightforward to model using DFT.⁹⁵ Our DFT calculations on the RP3 phase reported here reveal only a small difference (0.02 eV) between predicted ground-state energies for the FM and the A-type AF long-range orders, which may indicate frustration caused by competing exchange interactions is a realistic conclusion in our materials. Interestingly, the DFT study of Lan et al. on the Ca-based *n* = 3 phases $\text{La}_{3-3x}\text{Ca}_{1+3x}\text{Mn}_3\text{O}_{10}$ also shows that in the doping range $0.39 < x < 0.96$ the FM and AF ground states closely compete energetically.⁷⁸ This is influenced by the differences in geometry and hence orbital occupation for the outer perovskite Mn ions (adjacent to a rock salt layer) and the inner Mn ions. This distinction between inner and outer Mn ions does not occur in the *n* = 1 or 2 structures, where there is a single Mn site. We investigated the differing environments of the inner and outer Mn ions in the two structures used for DFT calculations, which are shown in Figure 5, by calculating the bond valence sum (BVS) for each Mn ion, as well as for the Mn ions in the RP2 structure of corresponding composition (note the calculated M–O bond lengths are given in the Supporting Information, Table S1). In the RP3 mixed R site structure, the BVS for the inner Mn was 3.42 as compared to the outer Mn, which was 3.37. In comparison, for the RP2 mixed R site structure, the Mn ion had a BVS of 3.37. In all cases, the calculated BVS for the as-deposited A site ordering was within 0.01 of the mixed R site value. This indicates that the different A site orderings considered here have only a small effect on the coordination environment of the Mn ions. It is clear, however, that there is a significant difference in the coordination geometry of the inner and outer Mn ions within the *n* = 3

perovskite trilayer, which may drive the magnetic frustration observed. It appears then that for the $n = 3$ RP phases, the region of glassy magnetic ground state caused by competing FM and AF interactions occurs in a region of the phase diagram different from the $n = 2$ phase. It is possible that the prevailing magnetic ground state at $x = 0.33$ alternates with increasing n , forming a SG like state for $n = \text{odd}$ and a FM state for $n = \text{even}$. Further work on higher members of this LSMO-based RP series must be undertaken to determine this.

Of course, comparison of thin film and bulk magnetism is complicated by a number of factors. Epitaxial strain is known to substantially affect ordering temperatures and can introduce magnetic anisotropy where it is not present in the bulk.^{39,45,46,61} Nonstoichiometry, either cation or anion, can be more difficult to detect in thin films and also materially affects the magnetic properties.^{21,59} Furthermore, artificially constructed materials, by the nature of their synthesis, are likely to contain different concentrations and types of structural defects than single crystals or powders produced through other means. We have attempted to minimize the effects of all of these factors through selection of a low mismatch substrate, careful optimization of stoichiometric growth of the LSMO component and oxygen content of the RP films, and detailed structural characterization (including TEM and comparison with simulated XRD patterns). The lower Curie temperature of our LSMO monolayers as compared to the bulk may indicate some nonstoichiometry (either cation or anion), although other factors such as microstructure and grain boundary density may be important in determining T_C .⁹⁰ Our deposition of LSMO monolayers was under conditions optimal for RP3 deposition, and as such we did not seek to optimize the microstructure of thick LSMO films. As described above, no cation off stoichiometry was detected using EDX, and the lattice parameter of our RP3 films suggests the oxygen stoichiometry is close to nominal.

Another factor remains, which is the differing A site ordering. It appears from our TEM results that there is a distribution of A site orderings, with some regions having “mixed R site” ordering (Figure 4), some having the “as-deposited” order, and some showing random A cation distribution. The effect of these changes on the magnetic interactions of the Mn ions is unclear, but it may be to contribute to the disorder required for the formation of a glassy magnetic state.

CONCLUSION

Layer-by-layer growth by pulsed laser deposition gives access to the $n = 3$ member of the $(\text{SrO})(\text{La}_{0.67}\text{Sr}_{0.33}\text{MnO}_3)_n$ Ruddlesden–Popper series based on the LSMO colossal magnetoresistive perovskite. The growth of high-quality material is not guaranteed solely on the basis of the RHEED monitoring because of the ability of the structure to accommodate defects, with a range of diffraction patterns accessible with pure Ruddlesden–Popper unit cells. The A site ordering is largely controlled by the deposition kinetics, with a preference for the Sr^{2+} cations to occupy the 9 coordinate sites that is contrary to expectations based on bulk synthesis. The observed spin glass-like ground state is consistent with the competition between AF and FM ground states apparent from DFT calculations on the systems grown here. It is possible that an odd–even alternation between ferromagnetic and spin glass ground states occurs in this series, with the observed behavior displaying strong anisotropy and several temperature regimes arising from competing intra- and interlayer interactions, as

expected from the layered structure. These properties motivate the search for higher n members and alternative methods to control the A site ordering in this class of materials.

ASSOCIATED CONTENT

Supporting Information

Details of substrate preparation, RHEED response on growth of SrO on different surfaces, a comparison of interval and standard mode deposition of SrO, and tabulated Mn–O bond lengths derived from DFT calculations. This material is available free of charge via the Internet at <http://pubs.acs.org>.

AUTHOR INFORMATION

Corresponding Author

rossein@liv.ac.uk

Notes

The authors declare no competing financial interest.

ACKNOWLEDGMENTS

This work was supported by the European Research Council under the seventh Framework Program (FP7) (ERC Grant agreement 227987 RLUCIM). P.B. has received funding from the European Community’s 7th Framework Programme FP7/2007-2013 under Grant Agreement No. 214040. J.H. and M.B. acknowledge funding from the Research Foundation – Flanders under grant FWOG.0184.09N. H.T. acknowledges financial support of the GOA project “Xanes meets Elnes” of the University of Antwerp. J.V. acknowledges financial support from the European Research Council under the seventh Framework Program (FP7), ERC grant No. 246791 – COUNTATOMS. The Qu-Ant-EM microscope was partly funded by the Hercules fund from the Flemish Government. This research received financial support from the European Union under the Framework 6 program under a contract for an Integrated Infrastructure Initiative, Reference 026019ESTEEM.

REFERENCES

- Rijnders, G.; Koster, G.; Blank, D. H. A.; Rogalla, H. *Appl. Phys. Lett.* **1997**, *70*, 1888.
- Christen, H. M.; Eres, G. *J. Phys.: Condens. Matter* **2008**, *20*, 264005.
- Haeni, J. H.; Theis, C. D.; Schlom, D. G.; Tian, W.; Pan, X. Q.; Chang, H.; Takeuchi, I.; Xiang, X. D. *Appl. Phys. Lett.* **2001**, *78*, 3292.
- Perucchi, A.; Baldassarre, L.; Nucara, A.; Calvani, P.; Adamo, C.; Schlom, D. G.; Orgiani, P.; Maritato, L.; Lupi, S. *Nano Lett.* **2010**, *10*, 4819.
- Tian, W.; Pan, X. Q.; Haeni, J. H.; Schlom, D. G. *J. Mater. Res.* **2001**, *16*, 2013.
- Ueda, K.; Tabata, H.; Kawai, T. *Science* **1998**, *280*, 1064.
- Izumi, M.; Murakami, Y.; Konishi, Y.; Manako, T.; Kawasaki, M.; Tokura, Y. *Phys. Rev. B* **1999**, *60*, 1211.
- Warusawithana, M. P.; Colla, E. V.; Eckstein, J. N.; Weissman, M. B. *Phys. Rev. Lett.* **2003**, *90*, 036802.
- Bousquet, E.; Dawber, M.; Stucki, N.; Lichtensteiger, C.; Hermet, P.; Gariglio, S.; Triscone, J. M.; Ghosez, P. *Nature* **2008**, *452*, 732.
- May, S. J.; Ryan, P. J.; Robertson, J. L.; Kim, J. W.; Santos, T. S.; Karapetrova, E.; Zarestky, J. L.; Zhai, X.; te Velthuis, S. G. E.; Eckstein, J. N.; Bader, S. D.; Bhattacharya, A. *Nat. Mater.* **2009**, *8*, 892.
- Yan, L.; Niu, H. J.; Duong, G. V.; Suchomel, M. R.; Bacsa, J.; Chalker, P. R.; Hadermann, J.; van Tendeloo, G.; Rosseinsky, M. J. *Chem. Sci.* **2011**, *2*, 261.
- Yan, L.; Niu, H. J.; Bridges, C. A.; Marshall, P. A.; Hadermann, J.; van Tendeloo, G.; Chalker, P. R.; Rosseinsky, M. J. *Angew. Chem., Int. Ed.* **2007**, *46*, 4539.

- (13) Tian, W.; Haeni, J. H.; Schlom, D. G.; Hutchinson, E.; Sheu, B. L.; Rosario, M. M.; Schiffer, P.; Liu, Y.; Zurbuchen, M. A.; Pan, X. Q. *Appl. Phys. Lett.* **2007**, *90*, 202507.
- (14) Battle, P. D.; Cox, D. E.; Green, M. A.; Millburn, J. E.; Spring, L. E.; Radaelli, P. G.; Rosseinsky, M. J.; Vente, J. F. *Chem. Mater.* **1997**, *9*, 1042.
- (15) Chauvet, O.; Goglio, G.; Molinie, P.; Corraze, B.; Brohan, L. *Phys. Rev. Lett.* **1998**, *81*, 1102.
- (16) Kimura, T.; Tokura, Y. *Annu. Rev. Mater. Sci.* **2000**, *30*, 451.
- (17) Kubota, M.; Fujioka, H.; Hirota, K.; Ohoyama, K.; Moritomo, Y.; Yoshizawa, H.; Endoii, Y. *J. Phys. Soc. Jpn.* **2000**, *69*, 1606.
- (18) Larochelle, S.; Mehta, A.; Lu, L.; Mang, P. K.; Vajk, O. P.; Kaneko, N.; Lynn, J. W.; Zhou, L.; Greven, M. *Phys. Rev. B* **2005**, *71*, 024435.
- (19) Lee, J. S.; Kao, C. C.; Nelson, C. S.; Jang, H.; Ko, K. T.; Kim, S. B.; Choi, Y. J.; Cheong, S. W.; Smadici, S.; Abbamonte, P.; Park, J. H. *Phys. Rev. Lett.* **2011**, *107*, 037206.
- (20) Potter, C. D.; Swiatek, M.; Bader, S. D.; Argyriou, D. N.; Mitchell, J. F.; Miller, D. J.; Hinks, D. G.; Jorgensen, J. D. *Phys. Rev. B* **1998**, *57*, 72.
- (21) Kawano, S.; Achiwa, N.; Kamegashira, N.; Aoki, M. *J. Phys.* **1988**, *49*, 829.
- (22) Mitchell, J. F.; Argyriou, D. N.; Berger, A.; Gray, K. E.; Osborn, R.; Welp, U. *J. Phys. Chem. B* **2001**, *105*, 10731.
- (23) Tanaka, H.; Kawai, T. *Appl. Phys. Lett.* **2000**, *76*, 3618.
- (24) Nelson-Cheeseman, B. B.; Shah, A. B.; Santos, T. S.; Bader, S. D.; Zuo, J. M.; Bhattacharya, A. *Appl. Phys. Lett.* **2011**, *98*, 072505.
- (25) Cha, L. M.; Zhang, P. X.; Habermeier, H. U. *Acta Phys. Sin.* **2003**, *52*, 498.
- (26) Konishi, Y.; Kimura, T.; Izumi, M.; Kawasaki, M.; Tokura, Y. *Appl. Phys. Lett.* **1998**, *73*, 3004.
- (27) Tiwari, A.; Narayan, J.; Sudhakar, N.; Rajeev, K. P. *Solid State Commun.* **2004**, *132*, 863.
- (28) Matvejeff, M.; Chikyow, T.; Lippmaa, M. *J. Cryst. Growth* **2009**, *311*, 1201.
- (29) Matvejeff, M.; Yoshimatsu, K.; Kumigashira, H.; Oshima, M.; Lippmaa, M. *Appl. Phys. Lett.* **2009**, *95*, 152110.
- (30) Lmouchter, M.; Iwayama, M.; Tanaka, Y.; Suzuki, M. *Jpn. J. Appl. Phys., Part 1* **2005**, *44*, 6016.
- (31) Siwach, P. K.; Singh, H. K.; Srivastava, O. N. *J. Phys. D: Appl. Phys.* **2006**, *39*, 3731.
- (32) Takamura, Y.; Grepstad, J. K.; Chopdekar, R. V.; Suzuki, Y.; Marshall, A. F.; Zheng, H.; Mitchell, J. F. *Appl. Phys. Lett.* **2005**, *87*, 142508.
- (33) Koster, G.; Kropman, B. L.; Rijnders, G.; Blank, D. H. A.; Rogalla, H. *Appl. Phys. Lett.* **1998**, *73*, 2920.
- (34) Yee, S. M. M.; Crandles, D. A.; Goncharova, L. V. *J. Appl. Phys.* **2011**, *110*, 033906.
- (35) Kresse, G.; Furthmuller, J. *Phys. Rev. B* **1996**, *54*, 11169.
- (36) Perdew, J. P.; Burke, K.; Ernzerhof, M. *Phys. Rev. Lett.* **1997**, *78*, 1396.
- (37) Kresse, G.; Joubert, D. *Phys. Rev. B* **1999**, *59*, 1758.
- (38) Urushibara, A.; Moritomo, Y.; Arima, T.; Asamitsu, A.; Kido, G.; Tokura, Y. *Phys. Rev. B* **1995**, *51*, 14103.
- (39) Zheng, B.; Binggeli, N. *J. Phys.: Condens. Matter* **2009**, *21*, 115602.
- (40) Henzler, M. *Surf. Sci.* **1996**, *357–358*, 809.
- (41) Maurice, J.-L.; Pailloux, F.; Barthelemy, A.; Durand, O.; Imhoff, D.; Lyonnet, R.; Rocher, A.; Contour, J.-P. *Philos. Mag.* **2003**, *83*, 3201.
- (42) Ranno, L.; Llobet, A.; Tiron, R.; Favre-Nicolin, E. *Appl. Surf. Sci.* **2002**, *188*, 170.
- (43) Dho, J.; Hur, N. H.; Kim, I. S.; Park, Y. K. *J. Appl. Phys.* **2003**, *94*, 7670.
- (44) Tsui, F.; Smoak, M. C.; Nath, T. K.; Eom, C. B. *Appl. Phys. Lett.* **2000**, *76*, 2421.
- (45) Haghiri-Gosnet, A. M.; Wolfman, J.; Mercey, B.; Simon, C.; Lecoeur, P.; Korzenki, M.; Hervieu, M.; Desfeux, R.; Baldinozzi, G. J. *Appl. Phys.* **2000**, *88*, 4257.
- (46) Yang, Z.; Sun, L.; Ke, C.; Chen, X.; Zhu, W.; Tan, O. *J. Cryst. Growth* **2009**, *311*, 3289.
- (47) Sun, J. Z.; Abraham, D. W.; Roche, K.; Parkin, S. S. P. *Appl. Phys. Lett.* **1998**, *73*, 1008.
- (48) Petrisor, T.; Gabor, M. S.; Boulle, A.; Bellouard, C.; Tiusan, C.; Pana, O. *J. Appl. Phys.* **2011**, *109*, 123913.
- (49) Hawley, M. E.; Brown, G. W.; Yashar, P. C.; Kwon, C. *J. Cryst. Growth* **2000**, *211*, 86.
- (50) Vlakhov, E. S.; Donchev, T. I.; Spasov, A. Y.; Dorr, K.; Nenkov, K. A.; Handstein, A.; Pignard, S.; Vincent, H. *Vacuum* **2003**, *69*, 249.
- (51) Sukhorukov, Y. P.; Nosov, A. P.; Loshkareva, N. N.; Mostovshchikova, E. V.; Telegin, A. V. *J. Appl. Phys.* **2005**, *97*, 103710.
- (52) Takahashi, R.; Matsumoto, Y.; Ohsawa, T.; Lippmaa, M.; Kawasaki, M.; Koinuma, H. *J. Cryst. Growth* **2002**, *234*, 505.
- (53) Jang, H. W.; et al. *Science* **2011**, *331*, 886.
- (54) Blank, D. H. A.; Koster, G.; Rijnders, G.; van Setten, E.; Slycke, P.; Rogalla, H. *Appl. Phys. A: Mater. Sci. Process.* **1999**, *69*, S17.
- (55) Blank, D. H. A.; Koster, G.; Rijnders, G.; van Setten, E.; Slycke, P.; Rogalla, H. *J. Cryst. Growth* **2000**, *211*, 98.
- (56) Koster, G.; Verbist, K.; Rijnders, G.; Rogalla, H.; van Tendeloo, G.; Blank, D. H. A. *Phys. C (Amsterdam, Neth.)* **2001**, *353*, 167.
- (57) Battle, P. D.; Green, M. A.; Laskey, N. S.; Millburn, J. E.; Murphy, L.; Rosseinsky, M. J.; Sullivan, S. P.; Vente, J. F. *Chem. Mater.* **1997**, *9*, 552.
- (58) Sloan, J.; Battle, P. D.; Green, M. A.; Rosseinsky, M. J.; Vente, J. F. *J. Solid State Chem.* **1998**, *138*, 135.
- (59) Ohnishi, T.; Shibuya, K.; Yamamoto, T.; Lippmaa, M. *J. Appl. Phys.* **2008**, *103*, 103703.
- (60) Orgiani, P.; Petrov, A. Y.; Ciancio, R.; Galdi, A.; Maritato, L.; Davidson, B. A. *Applied Physics Letters* **2012**, *100*, 042404.
- (61) Du, Y. S.; Wang, B.; Li, T.; Yu, D. B.; Yan, H. *J. Magn. Magn. Mater.* **2006**, *297*, 88.
- (62) Moritomo, Y.; Asamitsu, A.; Kuwahara, H.; Tokura, Y. *Nature* **1996**, *380*, 141.
- (63) Ganguly, P.; Rao, C. N. R. *J. Solid State Chem.* **1984**, *53*, 193.
- (64) Rao, C. N. R.; Ganguly, P.; Singh, K. K.; Ram, R. A. M. *J. Solid State Chem.* **1988**, *72*, 14.
- (65) Moritomo, Y.; Tomioka, Y.; Asamitsu, A.; Tokura, Y.; Matsui, Y. *Phys. Rev. B* **1995**, *51*, 3297.
- (66) Hur, T.-B.; Hwang, Y.-H.; Kim, H.-K.; Park, H.-L. *J. Appl. Phys.* **2004**, *96*, 1740.
- (67) Heinke, H.; Moller, M. O.; Hommel, D.; Landwehr, G. *J. Cryst. Growth* **1994**, *135*, 41.
- (68) Kennedy, R. J.; Stampe, P. A. *J. Cryst. Growth* **1999**, *207*, 200.
- (69) Battle, P. D.; Green, M. A.; Lago, J.; Millburn, J. E.; Rosseinsky, M. J.; Vente, J. F. *Chem. Mater.* **1998**, *10*, 658.
- (70) Jonason, K.; Vincent, E.; Hammann, J.; Bouchaud, J. P.; Nordblad, P. *Phys. Rev. Lett.* **1998**, *81*, 3243.
- (71) Jonsson, P. E.; Rice, S. A. *Adv. Chem. Phys.* **2004**, *128*, 191.
- (72) Palmer, R. G.; Stein, D. L.; Abrahams, E.; Anderson, P. W. *Phys. Rev. Lett.* **1984**, *53*, 958.
- (73) Chamberlin, R. V.; Mozurkewich, G.; Orbach, R. *Phys. Rev. Lett.* **1984**, *52*, 867.
- (74) Itoh, M.; Natori, I.; Kubota, S.; Motoya, K. *J. Phys. Soc. Jpn.* **1994**, *63*, 1486.
- (75) Hashimoto, T.; Kojima, Y.; Ikegami, T.; Yamada, I. *J. Magn. Magn. Mater.* **1980**, *15–18*, 227.
- (76) Ito, A.; Torikai, E.; Morimoto, S.; Aruga, H.; Kikuchi, M.; Syono, Y.; Takei, H. *J. Phys. Soc. Jpn.* **1990**, *59*, 829.
- (77) Yeshurun, Y.; Tholence, J. L.; Kjems, J. K.; Wanklyn, B. *J. Phys. C: Solid State Phys.* **1985**, *18*, L483.
- (78) Lan, X.; Zhang, W. Y. *Eur. Phys. J. B* **2008**, *66*, 321.
- (79) Yu, R. C.; Li, S. Y.; Zhu, J. L.; Li, F. Y.; Zhang, Z.; Jin, C. Q.; Voigt-Martin, I. G. *J. Appl. Phys.* **2001**, *90*, 6302.
- (80) Yu, R. C.; Li, S. Y.; Zhu, J. L.; Li, F. Y.; Zhang, Z.; Jin, C. Q.; Voigt-Martin, I. G. *J. Phys.: Condens. Matter* **2002**, *14*, 11119.
- (81) Zubkov, V. G.; Tyutyunnik, A. P.; Berger, I. F.; Voronin, V. I.; Bazuev, G. V.; Moore, C. A.; Battle, P. D. *J. Solid State Chem.* **2002**, *167*, 453.

- (82) Rossell, H. J.; Goodman, P.; Bulcock, S.; March, R. H.; Kennedy, S. J.; White, T. J.; Lincoln, F. J.; Murray, K. S. *Aust. J. Chem.* **1996**, *49*, 205.
- (83) Floros, N.; Hervieu, M.; van Tendeloo, G.; Michel, C.; Maignan, A.; Raveau, B. *Solid State Sci.* **2000**, *2*, 1.
- (84) Tang, Y. K.; Ma, X.; Kou, Z. Q.; Sun, Y.; Di, N. L.; Cheng, Z. H.; Li, Q. A. *Phys. Rev. B* **2005**, *72*, 132403.
- (85) Asano, H.; Hayakawa, J.; Matsui, M. *Phys. Rev. B* **1998**, *57*, 1052.
- (86) Witte, N. S.; Goodman, P.; Lincoln, F. J.; March, R. H.; Kennedy, S. J. *Appl. Phys. Lett.* **1998**, *72*, 853.
- (87) Yang, H.; Tang, Y. K.; Yao, L. D.; Zhang, W.; Li, Q. A.; Li, F. Y.; Jin, C. Q.; Yu, R. C. *J. Alloys Compd.* **2008**, *454*, 1.
- (88) Yao, L. D.; Yang, H.; Zhang, W.; Li, F. Y.; Jin, C. Q.; Yu, R. C. *J. Appl. Phys.* **2006**, *100*, 023907.
- (89) Mahesh, R.; Mahendiran, R.; Raychaudhuri, A. K.; Rao, C. N. R. *J. Solid State Chem.* **1996**, *122*, 448.
- (90) Chai, P.; Liu, X. J.; Liu, Y.; Lv, M. F.; Meng, J. *J. Solid State Chem.* **2010**, *183*, 676.
- (91) Chen, R. J.; Greenblatt, M.; Bendersky, L. A. *Chem. Mater.* **2001**, *13*, 4094.
- (92) Reutler, P.; Friedt, O.; Buchner, B.; Braden, M.; Revcolevschi, A. *J. Cryst. Growth* **2003**, *249*, 222.
- (93) Baumann, C.; Allodi, G.; Buchner, B.; De Renzi, R.; Reuder, P.; Revcolevschi, A. *Phys. B: Condens. Matter* **2003**, *326*, 505.
- (94) Welp, U.; Berger, A.; Vlasko-Vlasov, V. K.; You, H.; Gray, K. E.; Mitchell, J. F. *J. Appl. Phys.* **2001**, *89*, 6621.
- (95) Binder, K.; Young, A. P. *Rev. Mod. Phys.* **1986**, *58*, 801.
- (96) Liu, X.; Jiao, Z.; Nakamura, K.; Hatano, T.; Zeng, Y. *J. Appl. Phys.* **2000**, *87*, 2431.